https://doi.org/10.5194/egusphere-2025-4800
Preprint. Discussion started: 13 November 2025

Two-Phase Thermal Simulation of Matrix Acidization Using the Non-Isothermal Darcy–Brinkman–Forchheimer Model

Yuanqing Wu[1], Jisheng Kou[2,3]

[1]School of Computer Science and Technology, Dongguan University of Technology, Dongguan 523808, Guangdong, China
[2]State Key Laboratory of Intelligent Deep Metal Mining and Equipment, Shaoxing University, Shaoxing 312000, Zhejiang, China
[3]Zhejiang Key Laboratory of Rock Mechanics and Geohazards， School of Civil Engineering, Shaoxing University, Shaoxing 312000, Zhejiang, China

Correspondence to: Jisheng Kou (jishengkou@163.com)

Abstract. This study presents a comprehensive two-phase thermal model for simulating matrix acidization in porous media using the non-isothermal Darcy–Brinkman–Forchheimer framework. The model integrates multiphase flow, reactive transport, dynamic porosity evolution, and heat transfer, with temperature-dependent reaction kinetics incorporated through an Arrhenius-type formulation. A series of numerical experiments are conducted to investigate the effects of initial matrix temperature, injected acid temperature, and injection velocity on dissolution behavior and wormhole formation. Results show that the initial matrix temperature has minimal influence due to rapid thermal equilibrium, while high acid temperature significantly enhances reaction rates and promote localized wormhole growth. Verification experiments confirm that increasing acid temperature produces effects similar to decreasing injection velocity, as both shift the dissolution pattern from uniform to ramified and wormhole-dominated regimes. These findings offer valuable insights for optimizing acidizing treatments by balancing thermal and hydrodynamic conditions to improve stimulation efficiency.

1. Introduction

Matrix acidizing is a widely used stimulation technique in the petroleum industry aimed at enhancing the productivity of hydrocarbon reservoirs, particularly in carbonate and sandstone formations. The process involves injecting reactive acid solutions—commonly hydrochloric acid—into the reservoir at pressures below the fracture pressure, allowing the acid to flow through the porous matrix and dissolve mineral components that block pore spaces. This dissolution improves the permeability of the formation, facilitating more efficient oil and gas flow to the wellbore. Matrix acidizing is especially important in carbonate reservoirs, where it can lead to the formation of high-conductivity channels known as wormholes, significantly boosting well performance. As a cost-effective and controllable stimulation method, matrix acidizing plays a crucial role in maximizing recovery from existing wells and extending the productive life of mature fields (Araújo et al., 2024; Mahdavi Kalatehno et al., 2025; Qureshi et al., 2023).

https://doi.org/10.5194/egusphere-2025-4800
Preprint. Discussion started: 13 November 2025

Numerical simulation is a crucial method for studying matrix acidizing. The evolution of numerical models for matrix acidizing can be summarized as follows: The earliest single-phase model, based on the Darcy scale, was introduced by (Daccord et al., 1993a, 1993b; Fredd and Fogler, 1998). (Golfier et al., 2002) later evaluated the Darcy-scale model's ability to capture different dissolution regimes and assess how flow parameters influence wormhole development. (Panga et al., 2005) advanced the field by proposing the two-scale model (Darcy scale and pore scale), which describes transport and reaction mechanisms in reactive dissolution and studies wormhole formation during carbonate core acidization. However, these models rely solely on Darcy's equation, which fails to accurately represent fluid dynamics in high-porosity regions that form during acidizing. As porosity increases—sometimes approaching unity in certain zones—Darcy's law becomes inadequate. Additionally, fluid velocities in these regions can rise significantly. To address this limitation, (Wu et al., 2015) introduced the Darcy-Brinkman-Forchheimer (DBF) model, incorporating Brinkman and Forchheimer terms into the momentum equations to better describe fluid dynamics in high-porosity conditions. Later, (Wu et al., 2022) combined the DBF framework with a continuum fracture model to simulate matrix acidization in fractured porous media, achieving accurate results with a simplified approach. The DBF framework has also been widely applied in other research areas, as seen in studies by (Alokaily, 2022; Deb et al., 2024; Shahid et al., 2025; Yoon and Mallikarjunaiah, 2025).

However, the models above assume a single water phase in the reservoir, with the acid dissolved within it. While single-phase models have been widely used in matrix acidizing studies due to their simplicity and computational efficiency, they exhibit severe limitations when applied to real reservoir conditions. A key drawback is the neglect of the oil phase, which is typically present in carbonate and sandstone formations during acidizing operations. This omission leads to an inability to capture essential two-phase flow dynamics, including capillary pressure, phase interference, and wettability-driven fluid redistribution—all of which critically influence acid accessibility and reaction efficiency (Rigi et al., 2025; Mahdavi Kalatehno et al., 2025). For example, in oil-wet systems, the presence of oil can hinder acid penetration into the matrix, modify dissolution patterns, and result in an underestimation of the pore volume required for breakthrough (Elsafih and Fahes, 2021). Additionally, single-phase models disregard saturation-dependent transport properties and chemical potential gradients, both of which play a vital role in accurately predicting wormhole development and treatment performance. While these simplified models are valuable for conceptual studies, their lack of two-phase physics limits their reliability for field-scale simulations and the optimization of acid stimulation treatments.

To address these challenges, researchers have developed two-phase two-scale continuum models by integrating traditional porous media flow theory with acidizing frameworks (Babaei and Sedighi, 2018; Wei et al., 2017). Notably, (Sabooniha et al., 2021) proposed a two-dimensional, two-phase model combining the Cahn–Hilliard phase-field theory with Navier–Stokes equations, solved numerically via the finite element method. Further advancing the field, (Ma et al., 2022) developed a three-dimensional two-phase acidizing model for fractured carbonate rocks, utilizing a unified pipe-network method alongside a sequential implicit time scheme and adaptive time-stepping to enhance simulation accuracy. A critical challenge in carbonate acidizing is the formation of highly permeable flow channels, which significantly alter flow dynamics due to the combined effects of fluid viscosity and inertia. While most

https://doi.org/10.5194/egusphere-2025-4800
Preprint. Discussion started: 13 November 2025

existing studies model these flows using Darcy's law alone, this approach neglects key factors such as viscous shear and inertial forces. A more robust alternative is the DBF model, which incorporates Darcy's law, the Brinkman term, and the Forchheimer correction, making it suitable for high-velocity flows and heterogeneous porous media. However, despite its advantages, the DBF model has been applied only to single-phase acidizing simulations (Kou et al., 2016, 2019; Wu and Ye, 2019), leaving its potential in two-phase systems unexplored. Thus, integrating the two-phase model with the DBF model is one contribution of this work.

The conventional DBF framework accounts only for mass and momentum conservation, neglecting the energy conservation equation. However, temperature variations—whether due to reservoir conditions or reaction heat—play a critical role in matrix acidizing. For instance, (Zhou et al., 2022) demonstrated that elevated temperatures significantly enhance the optimal acid injection rate, while (Jia et al., 2021) highlighted the pronounced influence of reaction temperature at higher injection rates. Their findings further indicate that the optimal injection rate decreases with increasing activation energy or decreasing acid diffusion coefficient, underscoring the necessity of incorporating thermal effects into acidizing models. To address this gap, (Wu et al., 2021) extended the single-phase DBF model by integrating the energy conservation equation, forming a thermal DBF framework capable of capturing temperature-dependent dynamics. However, this model remains limited by its single-phase assumption, restricting its applicability to real-world reservoir conditions, which typically involve multiphase flow. Therefore, this work advances the field by developing a novel two-phase thermal DBF model, representing a key contribution to the understanding of heat-fluid interactions in acidizing processes.

The proposed two-phase thermal DBF model addresses the limitations of traditional single-phase and isothermal frameworks by integrating several key physical mechanisms into a unified formulation. First, it incorporates multiphase momentum conservation by coupling the DBF equations with relative permeability functions, allowing for accurate representation of viscous and inertial effects in both water and oil phases. Second, it introduces energy conservation with interphase mass exchange, capturing heat transfer processes alongside acid–rock reactions and dissolution-induced phase changes. Third, the model features temperature-dependent reaction kinetics governed by Arrhenius-type relationships, enabling spatially resolved predictions of reaction rates under varying thermal conditions. Together, these components empower the model to simulate complex field phenomena with high fidelity, including thermally driven wormhole branching, rate optimization guided by thermal feedback, and quantification of competing effects between reaction enthalpy and viscous dissipation in multiphase systems. This work thus establishes the first comprehensive two-phase thermal DBF framework, effectively bridging the gap between idealized models and practical field applications where multiphase flow and thermal effects are inherently coupled. This work is organized as following.

Introduction: Presents the need for a thermal two-phase acidizing model to address limitations in existing single-phase or isothermal approaches.

Numerical Model: Formulates the coupled mass, momentum, energy, and species transport equations with temperature-dependent reaction kinetics.

Solution Procedure: Describes the discretization and solution procedure to implement the model.

Numerical Experiments: Shows some important conclusions from the numerical experiments.

https://doi.org/10.5194/egusphere-2025-4800
Preprint. Discussion started: 13 November 2025

Conclusion and Future Work: Summarizes key findings on how thermal and flow conditions govern acidizing efficiency. Outlines extensions to heterogeneous media, larger scales, multi-mineral systems, and optimization tools.

2. Numerical Model

The two-phase thermal DBF model includes the mass conservation equation for each fluid phase $\alpha \in \{w, n\}$, which is expressed as below. w represents the wetting phase such as the water phase, and n stands for the non-wetting phase such as the oil phase.

$$\frac{\partial(\phi S_\alpha)}{\partial t} + \nabla \cdot (\phi S_\alpha \boldsymbol{u_\alpha}) = 0, \tag{1}$$

In the equation, ϕ is the porosity, S_α is the saturation of phase α, $\boldsymbol{u_\alpha}$ is the effective velocity of phase α, and t is the time. This equation does not consider any source or sink term, and the fluid is incompressible. Based on the single-phase DBF equation, the DBF equation for the two-phase condition (the momentum conservation equation) is expressed as:

$$\rho_\alpha \left(\frac{\partial(\phi S_\alpha \boldsymbol{u_\alpha})}{\partial t} + \nabla \cdot (\phi S_\alpha \boldsymbol{u_\alpha} \otimes \boldsymbol{u_\alpha}) \right)$$

$$= -\nabla(p + \mu_\alpha) - \frac{\eta_\alpha \phi S_\alpha}{k_{r\alpha} \boldsymbol{K}} \boldsymbol{u_\alpha} + \nabla \cdot \phi S_\alpha \eta_\alpha \nabla \boldsymbol{u_\alpha} - \phi S_\alpha \rho_\alpha F_\alpha |\boldsymbol{u_\alpha}| \boldsymbol{u_\alpha} + \rho_\alpha \boldsymbol{g}, \tag{2}$$

where p is the fluid pressure, μ_α is the capillary pressure potential of phase α, η_α is the dynamic viscosity, $\boldsymbol{K}$ is the absolute permeability, $k_{r\alpha}$ is the relative permeability, ρ_α is the mass density of phase α, F_α is the Forchheimer drag coefficient, and $\boldsymbol{g}$ is the gravity. The fluid is assumed as the Newtonian fluids (constant viscosity). The chemical potential μ_α due to capillary effects is defined as (Kou et al., 2021,2023,2024):

$$\mu_w = \gamma_w \ln(S_w) + \gamma_{wn} S_n, \tag{3}$$

$$\mu_n = \gamma_n \ln(S_n) + \gamma_{wn} S_w, \tag{4}$$

with the saturation constraint

$$S_w + S_n = 1, \tag{5}$$

where γ_w, γ_n, and γ_{wn} are phenomenological constants related to fluid-fluid interactions. The transport of reactant (acid) concentration C_f in the wetting phase is governed by:

$$\frac{\partial(\phi S_w C_f)}{\partial t} + \nabla \cdot \left(\phi S_w \boldsymbol{u_w} C_f\right) - \nabla \cdot \left(\phi S_w \boldsymbol{D}_e \cdot \nabla C_f\right) = -\frac{S_w a_v k_s k_c C_f}{k_c + k_s}, \tag{6}$$

where $\boldsymbol{D}_e$ is the effective diffusivity, a_v is the specific surface area per unit volume, k_c, k_s are reaction rate constants for mass transfer and surface reaction, respectively. The porosity-progress equation is modeled as:

$$\frac{\partial \phi}{\partial t} = \frac{\alpha S_w a_v k_s k_c C_f}{\rho_s (k_c + k_s)}, \tag{7}$$

where ρ_s is the solid matrix density, α is a stoichiometric coefficient.

https://doi.org/10.5194/egusphere-2025-4800
Preprint. Discussion started: 13 November 2025

All the equations above are established with the constant-temperature assumption. However, it is known that temperature is an important factor to influence the chemical reaction in reservoirs. Thus, to consider the temperature effect, we introduce the energy conservation equation as following.

$$\sum_{\alpha=w,n} \rho_\alpha \theta_\alpha \frac{\partial(\phi S_\alpha T)}{\partial t} + \rho_s \theta_s \frac{\partial((1-\phi)T)}{\partial t} + \sum_{\alpha=w,n} \rho_\alpha \theta_\alpha \nabla \cdot (\phi S_\alpha \boldsymbol{v_\alpha} T)$$
$$-\nabla \cdot (\phi S_w M_w + \phi S_n M_n + (1-\phi) M_s) \nabla T$$
$$= -2H_r a_v k_e C_f + \sum_{\alpha=w,n} \left(\frac{\eta_\alpha \phi S_\alpha}{k_{r\alpha} \boldsymbol{K}} |\boldsymbol{v_\alpha}|^2 + \eta_\alpha \phi S_\alpha |\nabla \boldsymbol{v_\alpha}|^2 + \phi S_\alpha \rho_\alpha F_\alpha |\boldsymbol{v_\alpha}|^3\right), \tag{8}$$

where T stands for the temperature, θ_α is the specific heat capacity of the phase α, M_α is the thermal conductivity of the phase α. H_r is the reaction heat, which is expressed as

$$H_r = -6846 + 8.038T - 0.00322T^2 - 870.3T^{-1}. \tag{9}$$

Besides that, k_e is a coefficient, which is defined as

$$k_e = \frac{2k_c k_s}{k_c + 2k_s}. \tag{10}$$

The value of the molecular diffusion coefficient d_m depends on the temperature directly, which is called the Arrhenius-type dependencies. It can be expressed as

$$d_m = d_{m0} \cdot e^{\frac{E_g}{R_g}\left(\frac{1}{T_0} - \frac{1}{T}\right)}. \tag{11}$$

The subscript "0" stands for the initial value. E_g is the activation energy, and R_g is the molar gas constant. Moreover, k_s also has the Arrhenius-type dependencies, which is expressed as

$$k_s = k_{s0} \cdot e^{\frac{E_g}{R_g}\left(\frac{1}{T_0} - \frac{1}{T}\right)}. \tag{12}$$

By the temperature-dependent parameters above, the reaction term in the concentration equation (6) and the porosity equation (7) are affected by the temperature.

The equations form a fully coupled, nonlinear system that integrates two-phase flow dynamics, momentum transport, reactive acid dissolution, porosity evolution, and temperature changes to accurately simulate wormhole formation during acidizing operations. Temperature effects are critically incorporated through Arrhenius-type dependencies for molecular diffusion (d_m) and surface reaction rates (k_s), which directly influence acid transport (via the acid concentration equation) and porosity development (via the porosity-progress equation). The evolving porosity then feeds back into the mass and momentum conservation equations by modifying permeability and pore structure parameters, while the computed flow velocities and reaction rates determine heat generation in the energy conservation equation. This bidirectional coupling creates a continuous feedback loop: updated temperature values alter reaction kinetics and transport properties, which in turn affect fluid flow and dissolution patterns. The model's ability to capture these complex thermo-hydro-chemical interactions enables precise prediction of wormhole propagation under realistic reservoir conditions, providing valuable insights for optimizing stimulation treatments through comprehensive parameter sensitivity analysis and performance evaluation.

In the system, S_w, ϕ, p, $\boldsymbol{u_\alpha}$, C_f and T are the main unknowns to be solved by the numerical schemes mentioned later. The other variables can be computed by the following equations. The Forchheimer drag coefficient is calculated as

https://doi.org/10.5194/egusphere-2025-4800
Preprint. Discussion started: 13 November 2025

$$F_\alpha = \frac{1.75}{\sqrt{150(S_\alpha \phi)^3}}. \tag{13}$$

The relative permeability is

$$k_{r\alpha} = {S_\alpha}^3. \tag{14}$$

$\boldsymbol{D_e}$ is expressed as

$$\boldsymbol{D_e} = \alpha_{OS} d_m \boldsymbol{I} + \frac{\|\boldsymbol{u_w}\|}{\phi S_w}(d_l \boldsymbol{E} + d_t \boldsymbol{E}^\perp). \tag{15}$$

In 2D condition,

$$\boldsymbol{E} = \frac{1}{\|\boldsymbol{u_w}\|^2}\begin{pmatrix} u_{wx}^2 & u_{wx}u_{wy} \\ u_{wy}u_{wx} & u_{wy}^2 \end{pmatrix}, \tag{16}$$

$$\boldsymbol{E}^\perp = \boldsymbol{I} - \boldsymbol{E}. \tag{17}$$

u_{wx}、u_{wy} stand for the wetting-phase velocity of the x- and y-directions, respectively. d_l and d_t stand for the longitudinal dispersion coefficient and the transverse dispersion coefficient, respectively.

$$d_l = \alpha_{OS} d_m + \frac{2\lambda_X \|\boldsymbol{u}\| r_p}{\phi}, \tag{18}$$

$$d_t = \alpha_{OS} d_m + \frac{2\lambda_T \|\boldsymbol{u}\| r_p}{\phi}. \tag{19}$$

α_{OS} is a constant depending on pore connectivity. λ_X and λ_T are constants depending on the structure of the medium. Besides that, there are Kozeny-Carman equations as below

$$\frac{K}{K_0} = \frac{\phi}{\phi_0}\left(\frac{\phi(1-\phi_0)}{\phi_0(1-\phi)}\right)^2, \tag{20}$$

$$\frac{r_p}{r_0} = \sqrt{\frac{K\phi_0}{K_0\phi}}, \tag{21}$$

$$\frac{a_v}{a_0} = \frac{\phi r_0}{\phi_0 r_p}. \tag{22}$$

If the matrix is homogeneous, the permeability value K can be represented as a scalar. Based on Eq. (20), K can be directly calculated once ϕ is known. Furthermore, by combining Eqs. (20) - (22), the parameter a_v can be expressed as a function of ϕ, enabling its determination. r_p is the pore radius. k_c is calculated from Eq. (23).

$$k_c = \frac{d_m}{2r_p}\left(Sh_\infty + 0.7\left(\frac{2\|\boldsymbol{u_w}\| r_p \rho_w}{\eta_w}\right)^{\frac{1}{2}}\left(\frac{\eta_w d_m}{\rho_w}\right)^{\frac{1}{3}}\right), \tag{23}$$

where Sh_∞ is the asymptotic Sherwood number.

3. Solution Procedure

The strongly coupled nonlinear equation system presents significant computational challenges due to its inherent complexity. To address this, we employ a structured numerical approach using a uniform grid with spatial resolutions Δx and Δy in the respective coordinate directions, along with uniform time steps Δt for temporal discretization. The solution adopts a staggered grid arrangement, with primary variables (water saturation S_w, porosity ϕ, pressure p, acid concentration C_f, and temperature T) stored at cell centers while phase velocities $\boldsymbol{u_\alpha}$ are defined at cell edges. Spatial approximations are carefully

https://doi.org/10.5194/egusphere-2025-4800
Preprint. Discussion started: 13 November 2025

implemented: harmonic averaging is applied for edge porosities and permeabilities using adjacent cell-center values, while arithmetic averaging is used for nodal porosity and saturation calculations. The scheme employs upwind discretization for both edge saturations and acid concentrations to ensure numerical stability. The gradients can be derived with the finite difference method. This conservative formulation maintains proper mass balance while effectively handling the complex coupling between multiphase flow, reactive transport, evolving porosity-permeability relationships, and temperature change that characterize the acidizing process.

To solve the coupled system, it is first necessary to define a consistent solution sequence for the primary unknowns. The porosity ϕ^{n+1} is updated first, as it is directly governed by the porosity evolution equation (Eq. (7)), which is relatively straightforward. A first-order backward Euler scheme is used for time discretization throughout the model. Applying this scheme to Eq. (7) allows for the explicit computation of the updated porosity at the beginning of each time step, where the superscript n denotes the previous time level. Once porosity is updated, the next step is to solve for the wetting-phase saturation S_w^{n+1}. This requires discretizing the wetting-phase mass conservation equation (Eq. (1)), which leads to a linear system in which S_w^{n+1} is the unknown. Solving this system yields the new saturation field. Following this, the model proceeds to solve for pressure p^{n+1} and phase velocities $\boldsymbol{u}_\alpha^{n+1}$ simultaneously, using a coupled formulation of the momentum and mass conservation equations. To do so, the mass conservation equations for both wetting and non-wetting phases are summed to yield a unified continuity equation:

$$\frac{\partial \phi}{\partial t} + \sum_{\alpha=w,n}(\nabla \cdot (\phi S_\alpha \boldsymbol{u}_\alpha)) = 0. \tag{24}$$

This equation, in combination with the momentum equation (Eq. (2)), is discretized to form a linear system in which the unknowns are p^{n+1} and $\boldsymbol{u}_\alpha^{n+1}$. Since the DBF momentum equation is nonlinear in velocity, appropriate linearization is performed: the advective term is approximated as $\nabla \cdot (\phi S_\alpha \boldsymbol{u}_\alpha^n \otimes \boldsymbol{u}_\alpha^{n+1})$, while the Forchheimer term is linearized as $\phi S_\alpha \rho_\alpha F_\alpha |\boldsymbol{u}_\alpha^n| \boldsymbol{u}_\alpha^{n+1}$. Once the velocity and pressure fields are updated, the acid concentration C_f^{n+1} is solved by discretizing the reactive transport equation (Eq. (6)), again yielding a linear system. The reaction source term is treated implicitly using values from the new time step. The final step in the solution sequence is the update of temperature T^{n+1}, governed by the energy conservation equation (Eq. (8)). Here, all temperature-dependent terms on the left-hand side are discretized implicitly (using T^{n+1}), while the source and transport terms on the right-hand side are discretized explicitly (using T^n). This approach yields a linear system for T^{n+1}, which can be solved to update the thermal field. This time-stepping procedure is repeated iteratively until either the final simulation time is reached or breakthrough occurs. Breakthrough is defined as the moment when the pressure drop between the inlet and outlet boundaries decreases to within 1% of its initial value, indicating the formation of a high-conductivity channel. It is important to ensure that all auxiliary variables are updated prior to their use in the computation of the primary unknowns.

High-resolution simulation of matrix acidizing in porous media requires fine computational grids to accurately resolve porosity heterogeneity and capture wormhole dynamics. However, the resulting large-scale systems significantly increase computational demand. To address this, an efficient parallel

https://doi.org/10.5194/egusphere-2025-4800
Preprint. Discussion started: 13 November 2025

computing strategy is developed, focusing on domain decomposition, inter-processor communication, and distributed solution of the coupled linear system. More details on the parallelization can be found in (Wu et al., 2015).

4. Numerical Experiments

4.1 Experiments with different initial matrix temperatures

To investigate the influence of the initial matrix temperature on two-phase acidizing, three numerical experiments are conducted, each with a constant acid injection temperature but different initial matrix temperatures. The injection temperature of the acid is maintained at 320 K, while the initial matrix temperatures are set to 320 K, 420 K, and 520 K, respectively. The computational domain is a rectangular matrix measuring 0.1 m × 0.1 m, discretized into a uniform grid of 40 × 40 cells. Initially, the matrix is nearly saturated with oil, with a water saturation of 0.01. Acid is injected from the left boundary at a constant velocity of 4.17×10^{-5} m/s, resulting in a water saturation of 1.0 at that boundary. The injected acid has a concentration of 500 mol/m^3. The right boundary serves as the outflow, while the top and bottom boundaries are impermeable. To represent natural heterogeneity, the initial porosity is spatially randomized with an average value of 0.18. Gravity is applied in the *y*-direction. The relevant physical and chemical parameters used in the simulations are summarized in **Table 1**. The simulation is performed with a time step of ten seconds, and the UMFPACK solver is employed for solving the resulting linear systems.

Table 1 Physical and chemical parameters of the experiments

Parameter	Value	Unit
a_{v0}	5.0×10^{-1}	m^{-1}
$C_{f,\mathrm{in}}$	5.0×10^{2}	$\mathrm{mol/m^3}$
d_{m0}	3.6×10^{-9}	$\mathrm{m^2/s}$
g_y	-9.807	$\mathrm{m/s^2}$
K_0	9.869233×10^{-16}	$\mathrm{m^2}$
k_{s0}	2.0×10^{-3}	$\mathrm{m/s}$
M_n	1.5×10^{1}	$\mathrm{W/(m \cdot K)}$
M_s	5.526×10^{2}	$\mathrm{W/(m \cdot K)}$
M_w	6.0×10^{1}	$\mathrm{W/(m \cdot K)}$
r_0	1.0×10^{-6}	m
Sh_∞	3.66	
α	5.0×10^{-2}	kg/mol
α_{OS}	5.0×10^{-1}	
γ_n	0.0	$\mathrm{Pa \cdot s}$
γ_w	5.8×10^{2}	$\mathrm{Pa \cdot s}$
γ_{wn}	0.0	$\mathrm{Pa \cdot s}$

https://doi.org/10.5194/egusphere-2025-4800
Preprint. Discussion started: 13 November 2025

$\boldsymbol{\eta_n}$	1.0×10^{-2}	$\mathrm{Pa \cdot s}$
$\boldsymbol{\eta_w}$	1.0×10^{-3}	$\mathrm{Pa \cdot s}$
$\boldsymbol{\theta_n}$	2.0×10^{2}	$\mathrm{J/(kg \cdot K)}$
$\boldsymbol{\theta_s}$	2.0×10^{1}	$\mathrm{J/(kg \cdot K)}$
$\boldsymbol{\theta_w}$	4.184×10^{2}	$\mathrm{J/(kg \cdot K)}$
$\boldsymbol{\lambda_T}$	1.0×10^{-1}	
$\boldsymbol{\lambda_X}$	5.0×10^{-1}	
$\boldsymbol{\rho_n}$	9.0×10^{2}	$\mathrm{kg/m^3}$
$\boldsymbol{\rho_s}$	2.71×10^{3}	$\mathrm{kg/m^3}$
$\boldsymbol{\rho_w}$	1.01×10^{3}	$\mathrm{kg/m^3}$
$\boldsymbol{\bar{\phi}_0}$	1.8×10^{-1}	

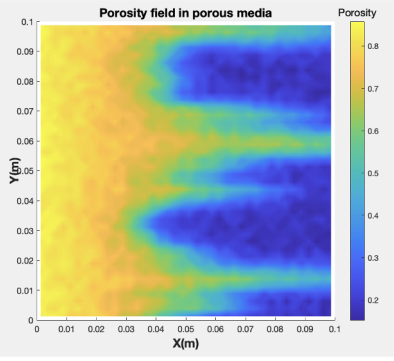

(a) Porosity profile with initial matrix temperature of 320 K.

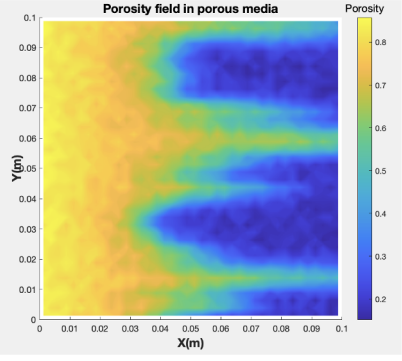

(b) Porosity profile with initial matrix temperature of 420 K.

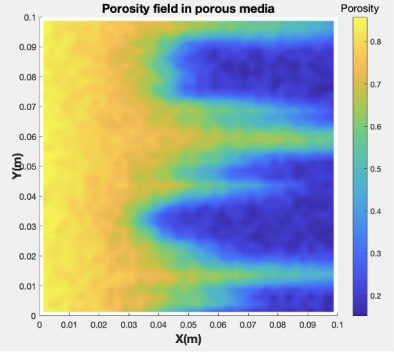

(c) Porosity profile with initial matrix temperature of 520 K.

Figure 1 Porosity profiles of the two-phase experiments at breakthrough with different initial matrix temperatures.

https://doi.org/10.5194/egusphere-2025-4800
Preprint. Discussion started: 13 November 2025

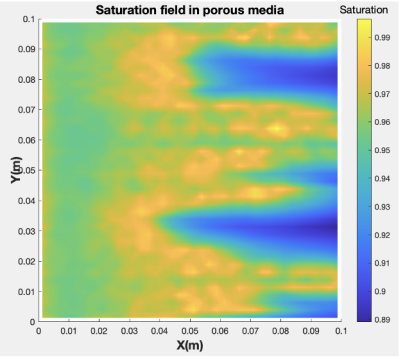

(a) Saturation profile with initial matrix temperature of 320 K.

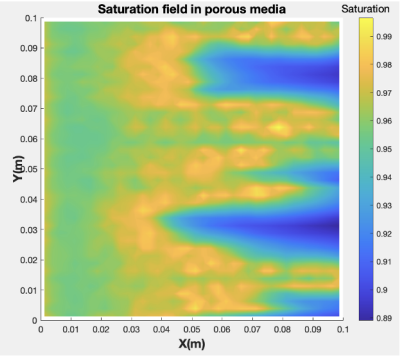

(b) Saturation profile with initial matrix temperature of 420 K.

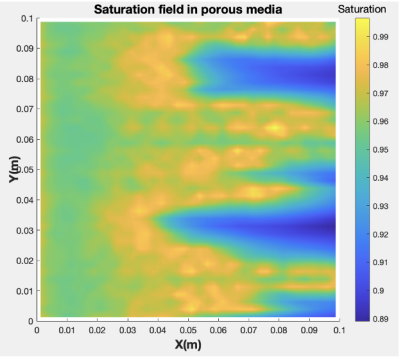

(c) Saturation profile with initial matrix temperature of 520 K.

Figure 2 Saturation profiles of the two-phase experiments at breakthrough with different initial matrix temperatures.

https://doi.org/10.5194/egusphere-2025-4800
Preprint. Discussion started: 13 November 2025

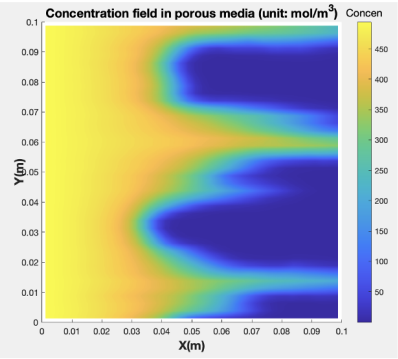

(a) Concentration profile with initial matrix temperature of 320 K.

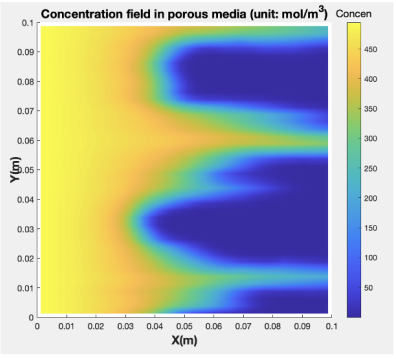

(b) Concentration profile with initial matrix temperature of 420 K.

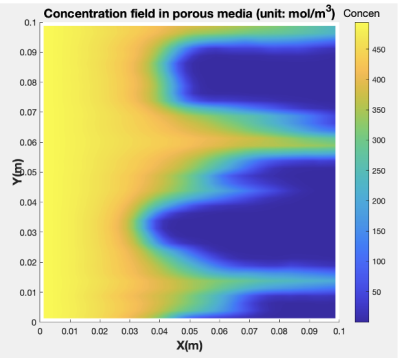

(c) Concentration profile with initial matrix temperature of 520 K.

Figure 3 Concentration profiles of the two-phase experiments at breakthrough with different initial matrix temperatures.

https://doi.org/10.5194/egusphere-2025-4800
Preprint. Discussion started: 13 November 2025

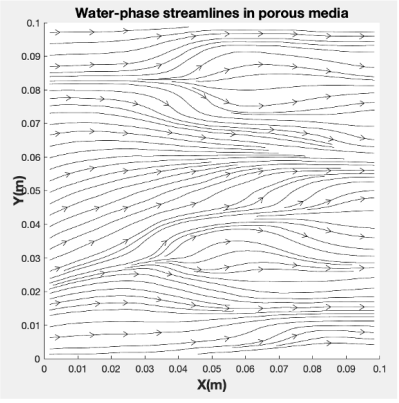

(a) Water-phase streamlines with initial matrix temperature of 320 K.

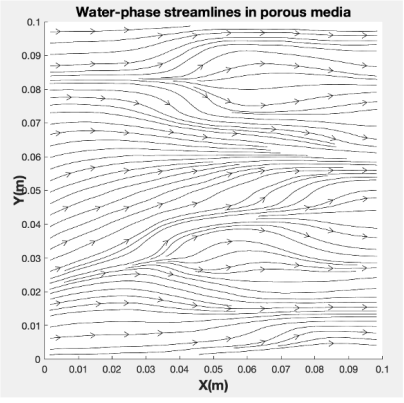

(b) Water-phase streamlines with initial matrix temperature of 420 K.

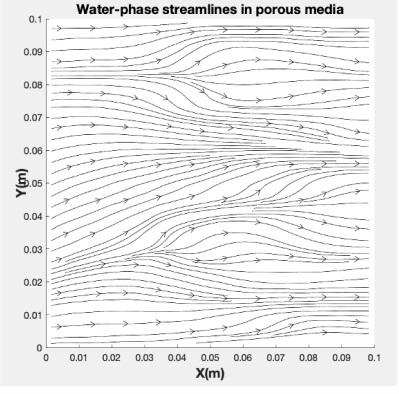

(c) Water-phase streamlines with initial matrix temperature of 520 K.

Figure 4 Water-phase streamlines of the two-phase experiments at breakthrough with different initial matrix temperatures.

https://doi.org/10.5194/egusphere-2025-4800
Preprint. Discussion started: 13 November 2025

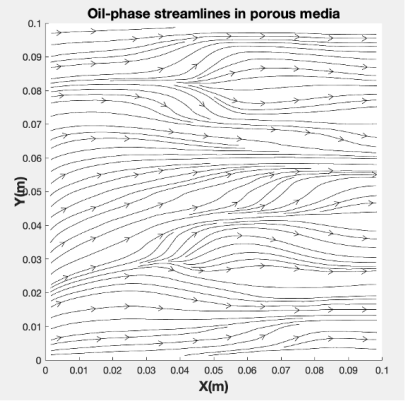

(a) Oil-phase streamlines with initial matrix temperature of 320 K.

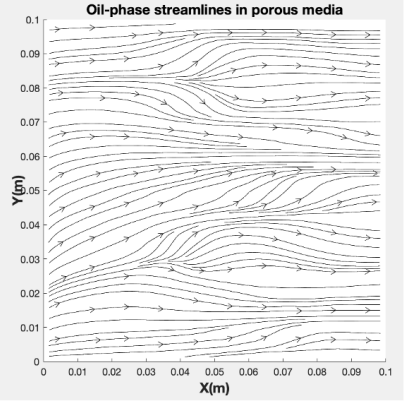

(b) Oil-phase streamlines with initial matrix temperature of 420 K.

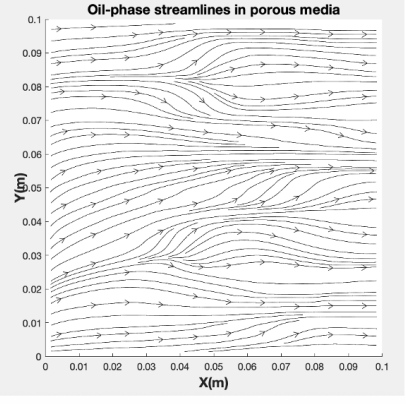

(c) Oil-phase streamlines with initial matrix temperature of 520 K.

Figure 5 Oil-phase streamlines of the two-phase experiments at breakthrough with different initial matrix temperatures.

https://doi.org/10.5194/egusphere-2025-4800
Preprint. Discussion started: 13 November 2025

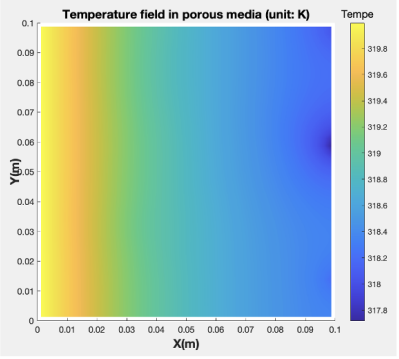

(a) Temperature profile with initial matrix temperature of 320 K.

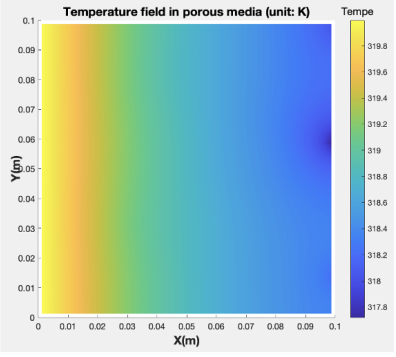

(b) Temperature profile with initial matrix temperature of 420 K.

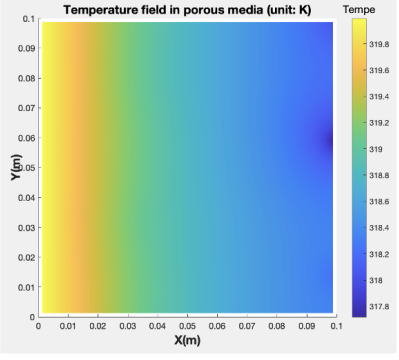

(c) Temperature profile with initial matrix temperature of 520 K.

Figure 6 Temperature profiles of the two-phase experiments at breakthrough with different initial matrix temperatures.

The numerical simulations reveal that variations in the initial matrix temperature—set at 320 K, 420 K, and 520 K—do not lead to significant differences in the outcome of the two-phase acidizing process. Across all three cases, the acid is injected at a constant temperature of 320 K, and the simulation is run until breakthrough, which occurs when the pressure differential between inlet and outlet stabilizes within 1% of its initial value. The computed pore volume to breakthrough (PVBT) is 6.61 in all scenarios, suggesting that the overall rate of acid propagation and dissolution behavior is largely insensitive to the initial thermal state of the matrix.

Figure 1 through **Figure 3** show that the porosity, saturation, and concentration profiles at breakthrough are highly similar across the three temperature settings. The acid-induced dissolution patterns develop with nearly identical wormhole morphologies, and the acid front progresses in a comparable manner through the porous medium. This indicates that, under the given conditions, the chemical reaction kinetics and transport processes are predominantly governed by the injected acid properties and flow dynamics, rather than the initial temperature of the solid matrix.

Similarly, **Figure 4** and **Figure 5**, which present the streamline patterns of the water and oil phases, show consistent flow structures in all cases. The injected acid solution follows the same preferential paths, displacing oil and generating high-permeability channels in a nearly identical fashion. The

https://doi.org/10.5194/egusphere-2025-4800
Preprint. Discussion started: 13 November 2025

similarity of these flow patterns reinforces the observation that the influence of initial matrix temperature is minimal in this two-phase system, at least under the conditions studied.

Finally, the temperature profiles shown in **Figure 6** confirm that although the initial matrix temperature is different, the overall thermal field at breakthrough converges toward a similar distribution. This is likely due to the dominance of the injected fluid temperature (320 K) and its thermal diffusion into the matrix. As a result, the initial temperature differences are progressively diminished during the acidizing process.

Overall, the results suggest that for this set of parameters, the initial matrix temperature has a negligible effect on the outcome of the acidizing process, including wormhole formation, fluid displacement, and breakthrough characteristics. This points to a degree of thermal robustness in the system, which could simplify operational strategies in real applications where subsurface temperature variations are present.

4.2 Experiments with different acid temperatures

Since the acidizing process shows minimal sensitivity to the initial matrix temperature, this section focuses on investigating the influence of the injected acid temperature on the acidizing behavior. The initial matrix temperature is fixed at 420 K, while the injection temperatures are varied, set at 290 K and 360 K, respectively. It is noted that the range of the acid temperature is generally between 273 K and 373 K in real applications, and therefore the acid temperatures outside the range are not considered. All other experimental conditions remain largely consistent with those described in the previous section.

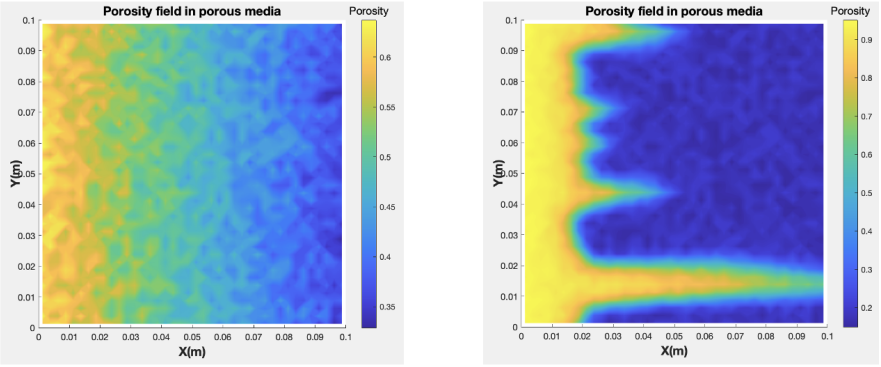

(a) Porosity profile with initial matrix temperature of 290 K. (b) Porosity profile with initial matrix temperature of 360 K.

Figure 7 Porosity profiles of the two-phase experiments at breakthrough with different acid temperatures.

https://doi.org/10.5194/egusphere-2025-4800
Preprint. Discussion started: 13 November 2025

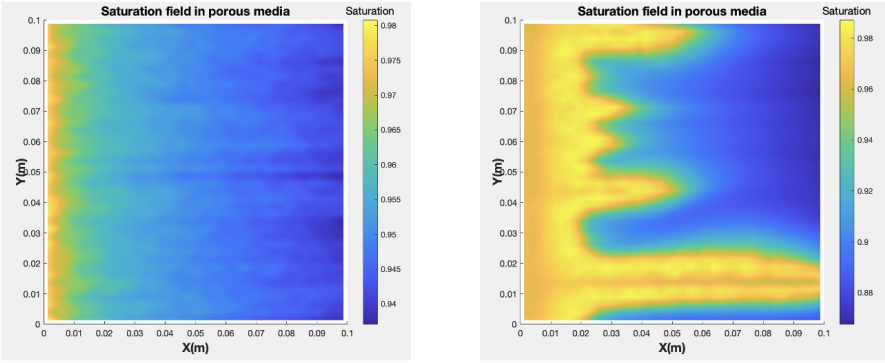

(a) Saturation profile with initial matrix temperature of 290 K. (b) Saturation profile with initial matrix temperature of 360 K.

Figure 8 Saturation profiles of the two-phase experiments at breakthrough with different acid temperatures.

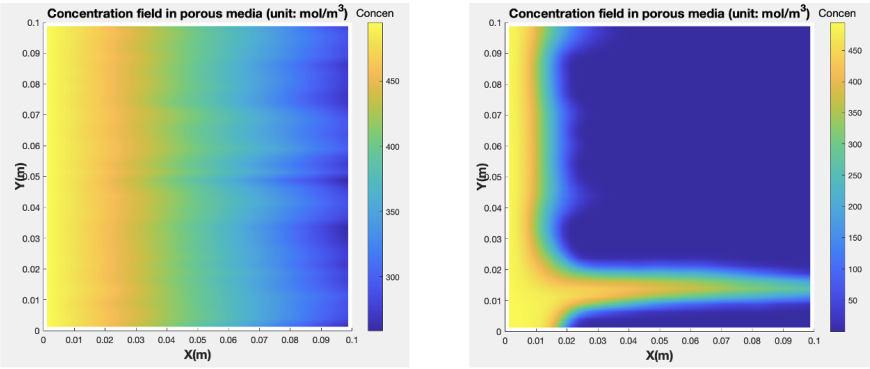

(a) Concentration profile with initial matrix temperature of 290 K. (b) Concentration profile with initial matrix temperature of 360 K.

Figure 9 Concentration profiles of the two-phase experiments at breakthrough with different acid temperatures.

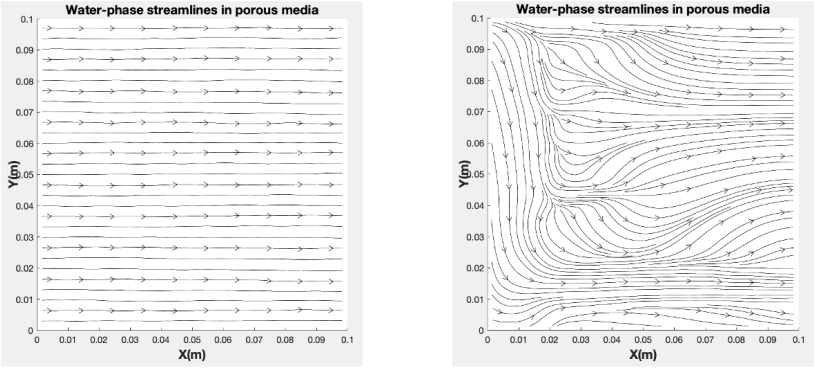

(a) Water-phase streamlines with initial matrix temperature of 290 K. (b) Water-phase streamlines with initial matrix temperature of 360 K.

Figure 10 Water-phase streamlines of the two-phase experiments at breakthrough with different acid temperatures.

https://doi.org/10.5194/egusphere-2025-4800
Preprint. Discussion started: 13 November 2025

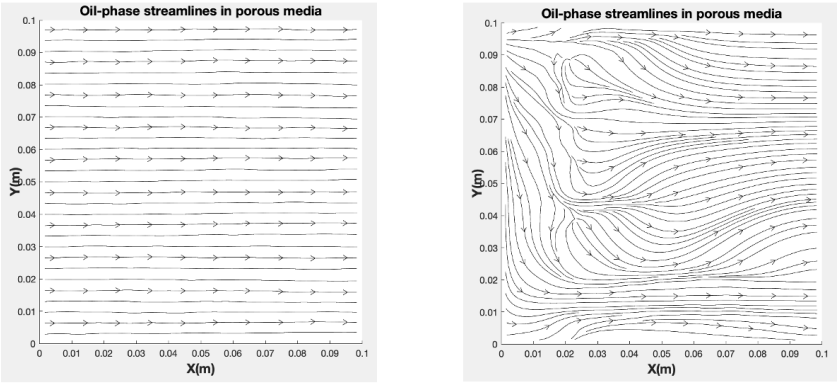

(a) Oil-phase streamlines with initial matrix temperature of 290 K. (b) Oil-phase streamlines with initial matrix temperature of 360 K.

Figure 11 Oil-phase streamlines of the two-phase experiments at breakthrough with different acid temperatures.

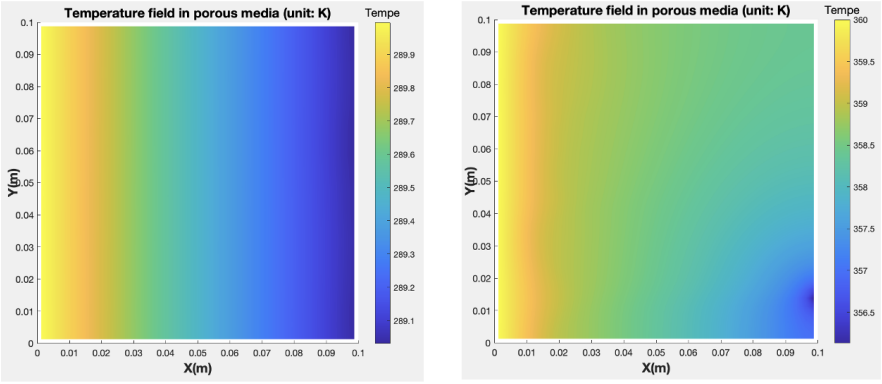

(a) Temperature profile with initial matrix temperature of 290 K. (b) Temperature profile with initial matrix temperature of 360 K.

Figure 12 Temperature profiles of the two-phase experiments at breakthrough with different acid temperatures.

This section explores the effect of injected acid temperature on the two-phase acidizing process while keeping the initial matrix temperature constant at 420 K. Three scenarios are examined: acid injection temperatures of 290 K, 320 K (from Section 4.1), and 360 K. The pore volume to breakthrough (PVBT) values corresponding to these cases are 10.96, 6.61, and 3.13, respectively. The results indicate a strong dependence of acidizing efficiency on the injected acid temperature. As the injection temperature increases, the PVBT significantly decreases, implying faster breakthrough and more efficient acid propagation through the matrix. This trend is attributed to the temperature dependence of the reaction kinetics—higher injection temperatures accelerate the acid–rock reaction rate, leading to faster porosity development, more rapid wormhole formation, and consequently earlier breakthrough.

Figure 7 and **Figure 8** present the porosity and saturation profiles at breakthrough for acid injection temperatures of 290 K and 360 K. At 360 K, dissolution is highly localized and concentrated, forming a well-developed wormhole structure. In contrast, the 290 K case exhibits a more diffuse and widespread dissolution front, indicative of slower reaction kinetics and reduced channeling efficiency.

https://doi.org/10.5194/egusphere-2025-4800
Preprint. Discussion started: 13 November 2025

This behavior corresponds to a uniform dissolution pattern, where acid interacts more evenly with the porous matrix rather than focusing along a dominant path. The corresponding saturation profiles further support this distinction. At 360 K, water displacement is strongly aligned with the main flow path, producing a narrow and well-defined saturation front. Conversely, the 290 K case shows a broader and more dispersed water front, reflecting the less focused nature of fluid transport under cooler acid injection conditions. For the intermediate case of 320 K (as discussed in Section 4.1), the porosity profile lies between the 290 K and 360 K cases. It displays several small branching fingers extending from the injection boundary, characteristic of a ramified dissolution pattern. According to (Wu, 2015), acidizing can produce five primary dissolution patterns—face, conical, wormhole, ramified, and uniform—depending primarily on the increase of the injection velocity, assuming other conditions remain constant. Interestingly, the observed trend suggests that increasing the injected acid temperature produces similar effects to decreasing the injection velocity, both leading to a transition from uniform toward wormhole-type dissolution. This highlights the dual role of thermal and hydrodynamic controls in shaping the acidizing outcome and suggests that temperature can be used as an alternative lever to optimize dissolution behavior in two-phase systems.

The acid concentration fields (**Figure 9**) further support these findings. At lower acid temperatures, acid is consumed more gradually and over a broader region, resulting in a more uniform concentration distribution. At 360 K, acid is rapidly consumed along the high-permeability wormhole, leading to a sharp depletion front and improved reactant utilization efficiency. The streamline patterns (**Figure 10** and **Figure 11**) also reflect the temperature-dependent channelization behavior. For the higher acid temperature (360 K), streamlines are strongly aligned with the wormhole path, concentrating both water and oil flow into narrow regions. This results in more focused displacement and enhanced acid penetration. At 290 K, streamlines are more dispersed, suggesting a less efficient fluid transport and weaker coupling between dissolution and flow. Finally, temperature profiles (**Figure 12**) illustrate how injected acid influences the thermal distribution in the matrix. At 360 K, the elevated injection temperature maintains a thermal gradient that sustains high reaction rates along the main channel. In contrast, the 290 K injection case shows a cooler and more diffused thermal field, contributing to lower reaction intensity.

In summary, the simulation results clearly demonstrate that the injected acid temperature plays a critical role in the efficiency of the acidizing process. Higher injection temperatures lead to accelerated reaction rates, more pronounced wormhole formation, and reduced PVBT values, indicating more efficient usage of the injected fluid. This finding highlights the importance of thermal management in designing effective acidizing strategies in two-phase flow systems.

4.3 Verification experiments

As discussed above, increasing the injected acid temperature appears to have an effect analogous to decreasing the injection velocity, particularly in terms of dissolution pattern and breakthrough behavior. To further examine this relationship, two additional simulations are conducted with varying injection velocities. In all previous experiments, the injection velocity was fixed at 4.17×10^{-5} m/s. In the new cases, the injection velocity is increased to 4.17×10^{-4} m/s and 1.0×10^{-3} m/s, respectively. The injected acid temperature is maintained at 360 K, and the initial matrix temperature remains at 420 K

https://doi.org/10.5194/egusphere-2025-4800
Preprint. Discussion started: 13 November 2025

for all scenarios. Thus, under the fixed thermal conditions, three different injection velocities are considered: 4.17×10^{-5} m/s, 4.17×10^{-4} m/s, and 1.0×10^{-3} m/s. The simulation results corresponding to the lowest velocity have already been presented in Section 4.2. The results for the two higher-velocity cases are provided and discussed in the following section.

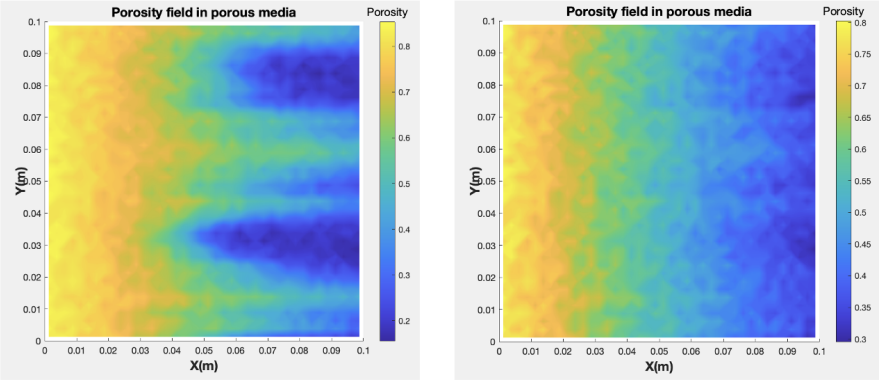

(a) Porosity profile with injection velocity of 4.17×10^{-4} m/s. (b) Porosity profile with injection velocity of 1.0×10^{-3} m/s.

Figure 13 Porosity profiles of the two-phase experiments at breakthrough with different injection velocity.

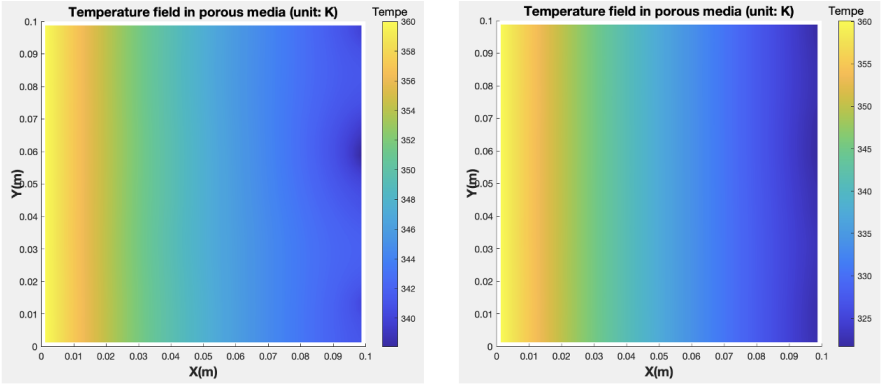

(a) Temperature profile with injection velocity of 4.17×10^{-4} m/s. (b) Temperature profile with injection velocity of 1.0×10^{-3} m/s.

Figure 14 Temperature profiles of the two-phase experiments at breakthrough with different injection velocity.

The porosity fields at breakthrough (**Figure 13**) reveal a distinct shift in the dissolution pattern as the injection velocity increases. At an injection velocity of 4.17×10^{-4} m/s, the dissolution exhibits a ramified pattern, characterized by multiple branching wormholes extending from the injection boundary. This morphology reflects a moderately efficient reaction front where several channels compete and develop simultaneously. In contrast, at the higher injection velocity of 1.0×10^{-3} m/s, the dissolution becomes more uniform, with acid spreading broadly across the domain and minimal evidence of localized channeling. This suggests that the elevated flow rate dilutes the acid–rock interaction front, preventing the formation of focused wormholes and instead promoting a diffuse dissolution regime. These observed transitions align well with the established classification of

https://doi.org/10.5194/egusphere-2025-4800
Preprint. Discussion started: 13 November 2025

dissolution patterns (face → conical → wormhole → ramified → uniform) as a function of increasing injection velocity (Wu, 2015). Specifically, the simulation with 4.17×10^{-4} m/s corresponds to the ramified regime, while the simulation with 1.0×10^{-3} m/s corresponds to the uniform regime. These findings reinforce the earlier conclusion that increasing the injected acid temperature has an effect analogous to decreasing the injection velocity, as both strategies favor more localized dissolution and efficient wormhole formation. The observations are summarized in **Table 2**.

The temperature fields (**Figure 14**) show that in both cases, the matrix is thermally dominated by the injected acid at 360 K, which progressively displaces the initially hotter matrix temperature of 420 K. The primary distinction lies in the temperature gradient: the simulation with 1.0×10^{-3} m/s exhibits a wider range between the maximum and minimum temperatures, indicating a more pronounced temperature gradient. This suggests that higher injection velocities enhance advective heat transport, leading to sharper thermal fronts across the domain.

Table 2 Dissolution patterns in different thermal and hydrodynamic conditions

Dissolution pattern	$\boldsymbol{T_{\text{injection acid}} = 360}$ **K** $\boldsymbol{T_{\text{initial matrix}} = 420}$ **K**	$\boldsymbol{v_{\text{injection acid}}} = 4.17 \times 10^{-5}$ m/s $\boldsymbol{T_{\text{initial matrix}} = 420}$ **K**
Uniform	$v_{\text{injection acid}} = 1.0 \times 10^{-3}$ m/s	$T_{\text{injection acid}} = 290$ **K**
Ramified	$v_{\text{injection acid}} = 4.17 \times 10^{-4}$ m/s	$T_{\text{injection acid}} = 320$ **K**
Wormhole	$v_{\text{injection acid}} = 4.17 \times 10^{-5}$ m/s	$T_{\text{injection acid}} = 360$ **K**

Overall, the results demonstrate that increasing the injection velocity leads to a transition from wormhole-like to ramified and eventually uniform dissolution patterns. This behavior confirms the earlier observation that raising acid temperature produces similar physical effects to lowering injection velocity, as both alter the balance between reaction and transport processes. These insights are critical for optimizing acidizing strategies, highlighting the importance of simultaneously managing temperature and flow rate to achieve the desired dissolution morphology and stimulation efficiency.

5. Conclusion and Future Work

In this work, we developed a novel two-phase thermal Darcy–Brinkman–Forchheimer (DBF) model to simulate matrix acidization processes in porous media under realistic reservoir conditions. The model integrates multiphase flow, reactive transport, heat transfer, and dynamic porosity evolution into a unified framework. Key contributions include the incorporation of temperature-dependent reaction kinetics via Arrhenius-type relationships, as well as a fully coupled numerical solution strategy that accounts for viscous, inertial, and thermal effects.

Numerical experiments were conducted to investigate the influence of initial matrix temperature, injected acid temperature, and injection velocity on the acidizing process. Results showed that the initial matrix temperature has minimal impact on wormhole formation and breakthrough behavior due to rapid thermal equilibration driven by acid injection. In contrast, the injected acid temperature significantly affects the dissolution pattern, reaction rate, and acid utilization efficiency. Higher

https://doi.org/10.5194/egusphere-2025-4800
Preprint. Discussion started: 13 November 2025

injection temperatures enhance reaction rates and promote localized wormhole formation, resulting in earlier breakthrough and reduced pore volume to breakthrough (PVBT).

Furthermore, verification simulations demonstrated that increasing acid temperature has a similar effect to decreasing injection velocity. Both approaches shift the dissolution regime from uniform to wormhole-dominated patterns, highlighting a fundamental coupling between thermal and hydrodynamic controls. These insights offer practical guidance for optimizing acidizing strategies by balancing thermal input and flow rate to improve treatment efficiency and control wormhole geometry.

While the current model provides a robust platform for simulating two-phase thermal acidizing, several directions remain for further enhancement. Future extensions will incorporate complex geological features such as natural fractures, vugs, and spatial heterogeneity in porosity and permeability. These additions will enable more realistic simulation of carbonate formations and fractured reservoirs. Moreover, the current study focuses on lab-scale domains. Scaling up the framework to field-scale models will require further optimization of the numerical solver, including parallel performance tuning and adaptive mesh refinement techniques. Besides that, incorporating multi-mineral reaction kinetics and competing acid–rock interactions (e.g., dolomite and calcite dissolution) will enhance the chemical fidelity of the model and broaden its applicability to various rock types. To better evaluate stimulation effectiveness, coupling the matrix acidizing model with wellbore dynamics and reservoir-scale production forecasting will be explored. Furthermore, data from high-fidelity simulations can be used to train surrogate models or integrate with machine learning algorithms for real-time optimization of injection schedules, temperature control, and acid composition.

These directions will further strengthen the capability of the proposed framework for practical reservoir engineering applications and enable more accurate design and evaluation of acidizing treatments in complex subsurface environments.

Code availability

Name of the code: Two-phase thermal DBF matrix acidizing simulator

Contact: wuyuanq@gmail.com, +86-13928772190

Hardware requirements: CPU: 2.2 GHz 6-Core Intel Core i7, Memory: 16 GB 2400 MHz DDR4

Program language: FORTRAN90, MATLAB, TECPLOT

Software required: LAPACK, UMFPACK, MUMPS, HYPRE, MPI

Program size: more than 10000 lines

The source codes are available for downloading at the link: https://doi.org/10.5281/zenodo.17272888 (Wu, 2025)

Author contribution

Wu: programming, the design and realization of the numerical experiments, the writing of the work. Kou: concepts of the work, the development of the numerical models, the algorithm design of the numerical scheme, the writing of the work.

https://doi.org/10.5194/egusphere-2025-4800
Preprint. Discussion started: 13 November 2025

Competing interests

The authors declare that they have no conflict of interest.

Acknowledgements

This manuscript was prepared with the assistance of ChatGPT, a language model developed by OpenAI, which was used for refining language. The authors have reviewed, revised and approved the final content.

References

Alokaily, S. A.: Numerical Simulations of Fluid Transport in Heterogeneous Darcy–Forchheimer–Brinkman Layers, Journal of Fluids Engineering, 144(12), 121404, https://doi.org/10.1115/1.4055072, 2022.

Araújo, E. D. A., Schwalbert, M. P., Leitão, R. J., & Aum, P. T. P.: Influence of Matrix-Acidizing Design on Oil Recovery and Economics in Carbonate Reservoirs Undergoing Waterflooding Offshore in Brazil, Energies, 17(4), 883, https://doi.org/10.3390/en17040883, 2024.

Babaei, M., & Sedighi, M.: Impact of phase saturation on wormhole formation in rock matrix acidizing, Chemical Engineering Science, 177, 39-52, https://doi.org/10.1016/j.ces.2017.10.046, 2018.

Daccord, G., Lenormand, R., & Lietard, O.: Chemical dissolution of a porous medium by a reactive fluid—I. Model for the "wormholing" phenomenon, Chemical Engineering Science, 48(1), 169-178, https://doi.org/10.1016/0009-2509(93)80293-Y, 1993. a

Daccord, G., Lietard, O., & Lenormand, R.: Chemical dissolution of a porous medium by a reactive fluid—II. Convection vs reaction, behavior diagram, Chemical engineering science, 48(1), 179-186, https://doi.org/10.1016/0009-2509(93)80294-Z, 1993. b

Deb, N., Farshi, M. S., Das, P. K., & Saha, S.: Convective flow optimization inside a lid-driven chamber with a rotating porous cylinder using Darcy–Brinkman–Forchheimer model, Journal of Thermal Analysis and Calorimetry, 149(12), 6125-6146, https://doi.org/10.1007/s10973-024-13228-y, 2024.

Elsafih, M., & Fahes, M.: Quantifying the effect of multiphase flow on matrix acidizing in oil-Bearing carbonate formations, SPE Production & Operations, 36(04), 795-806, https://doi.org/10.2118/205397-PA, 2021.

Fredd, C. N., & Fogler, H. S.: Influence of transport and reaction on wormhole formation in porous media, AIChE journal, 44(9), 1933-1949, https://doi.org/10.1002/aic.690440902, 1998.

Golfier, F., Zarcone, C., Bazin, B., Lenormand, R., Lasseux, D., & Quintard, M.: On the ability of a Darcy-scale model to capture wormhole formation during the dissolution of a porous medium, Journal of fluid Mechanics, 457, 213-254, https://doi.org/10.1017/S0022112002007735, 2002.

Jia, C., Sepehrnoori, K., & Yao, J.: Numerical studies and analysis on reactive flow in matrix acidizing coupled thermal-hydrological-mechanical-chemical processes, In ARMA US Rock Mechanics/Geomechanics Symposium (pp. ARMA-2021). ARMA, 2021 June.

Kou, J., Sun, S., & Wu, Y.: Mixed finite element-based fully conservative methods for simulating wormhole propagation, Computer Methods in Applied Mechanics and Engineering, 298, 279-302, https://doi.org/10.1016/j.cma.2015.09.015, 2016.

Kou, J., Sun, S., & Wu, Y.: A semi-analytic porosity evolution scheme for simulating wormhole propagation with the Darcy–Brinkman–Forchheimer model, Journal of Computational and Applied Mathematics, 348, 401-420, https://doi.org/10.1016/j.cam.2018.08.055, 2019.

https://doi.org/10.5194/egusphere-2025-4800
Preprint. Discussion started: 13 November 2025

Kou, J., Du, S., & Zhong, Z.: Energy stable modeling of two-phase flow in porous media with fluid–fluid friction force using a Maxwell-Stefan-Darcy approach, Physics of Fluids, 33, 073312, https://doi.org/10.1063/5.0053373, 2021.

Kou, J., Chen, H., Du, S., & Sun, S.: An efficient and physically consistent numerical method for the Maxwell-Stefan-Darcy model of two-phase flow in porous media, International Journal for Numerical Methods in Engineering, 124(3), 546-569, https://doi.org/10.1002/nme.7131, 2023.

Kou, J., Wang, X.: Numerical modeling of unsaturated flow in porous media using a thermodynamical approach, Capillarity, 11, 63-69, https://doi.org/10.46690/capi.2024.06.01, 2024.

Ma, G., Chen, Y., Wang, H., Li, T., & Nie, W.: Numerical analysis of two-phase acidizing in fractured carbonate rocks, Journal of Natural Gas Science and Engineering, 103, 104616, https://doi.org/10.1016/j.jngse.2022.104616, 2022.

Mahdavi Kalatehno, J., Khamehchi, E., Keihanikamal, M., Yousefmarzi, F., Dargi, M., & Daneshfar, P.: A successful case study of using HCl and viscoelastic diverting acid systems for carbonate matrix acidizing in an oil well with optimized predictive model, Journal of Petroleum Exploration and Production Technology, 15(1), 1, https://doi.org/10.1007/s13202-024-01896-3, 2025.

Panga, M. K., Ziauddin, M., & Balakotaiah, V.: Two‐scale continuum model for simulation of wormholes in carbonate acidization, AIChE journal, 51(12), 3231-3248, https://doi.org/10.1002/aic.10574, 2005.

Qureshi, U., Qureshi, H. A., Bhatti, A. A., Saeed, M. S., & Khalid, M. S.: Investigating the effects of matrix acidizing and acid fracturing on the production optimization of a carbonate reservoir: a case study, Arabian Journal of Geosciences, 16(11), 620, https://doi.org/10.1007/s12517-023-11734-1, 2023.

Sabooniha, E., Rokhforouz, M. R., Kazemi, A., & Ayatollahi, S.: Numerical analysis of two-phase flow in heterogeneous porous media during pre-flush stage of matrix acidizing: Optimization by response surface methodology, Physics of Fluids, 33(5), https://doi.org/10.1063/5.0046106, 2021.

Shahid, A., Wei, W., Abbas, T., & Bhatti, M. M.: A computational investigation of diffusivities and heat transfer in the flow of viscoelastic fluid through Darcy–Brinkman–Forchheimer medium, Numerical Heat Transfer, Part B: Fundamentals, 86(3), 762-779, https://doi.org/10.1080/10407790.2023.2296076, 2025.

Wei, W., Varavei, A., & Sepehrnoori, K.: Modeling and analysis on the effect of two-phase flow on wormhole propagation in carbonate acidizing, SPE Journal, 22(06), 2067-2083, https://doi.org/10.2118/186111-pa, 2017.

Wu, Y.: Parallel reservoir simulations with sparse grid techniques and applications to wormhole propagation, 2015.

Wu, Y. (2025). Two-phase thermal DBF matrix acidizing simulator. Zenodo. https://doi.org/10.5281/zenodo.17272888

Wu, Y., Kou, J., & Sun, S.: Matrix acidization in fractured porous media with the continuum fracture model and thermal Darcy-Brinkman-Forchheimer framework, Journal of Petroleum Science and Engineering, 211, 110210, https://doi.org/10.1016/j.petrol.2022.110210, 2022.

Wu, Y., Kou, J., Sun, S., & Wu, Y. S.: Thermodynamically consistent Darcy–Brinkman–Forchheimer framework in matrix acidization, Oil & Gas Science and Technology–Revue d'IFP Energies nouvelles, 76, 8, https://doi.org/10.2516/ogst/2020091, 2021.

Wu, Y., Salama, A., & Sun, S.: Parallel simulation of wormhole propagation with the Darcy–Brinkman–Forchheimer framework, Computers and Geotechnics, 69, 564-577, https://doi.org/10.1016/j.compgeo.2015.06.021, 2015.

https://doi.org/10.5194/egusphere-2025-4800
Preprint. Discussion started: 13 November 2025

Wu, Y., & Ye, M.: A Newton's second law abided Darcy-Brinkman-Forchheimer framework in matrix acidization simulation, In International Conference on Computational & Experimental Engineering and Sciences (pp. 861-866), Cham: Springer International Publishing, https://doi.org/10.1007/978-3-030-27053-7_73, 2019 March.

Yoon, H. C., & Mallikarjunaiah, S. M.: A stabilized finite element method for steady Darcy-Brinkman-Forchheimer flow model with different viscous and inertial resistances in porous media, arXiv preprint arXiv:2501.04041, 2025.

Zhou, L., Guo, A., Wang, X., Qiao, J., & Tang, X.: The effect of temperature, natural fractures and vugs on the acidizing process in fractured-vuggy reservoirs with hydro-thermal-chemical coupled modeling, Journal of Petroleum Science and Engineering, 213, 110416, https://doi.org/10.1016/j.petrol.2022.110416, 2022.